Supplementary Information

Dynamic observation of Mn-adatom mobility at perovskite oxide catalyst interfaces with water.

G. Lole et al.

1. Electrochemical characterization of epitaxial (001) oriented LSMO and PCMO electrodes

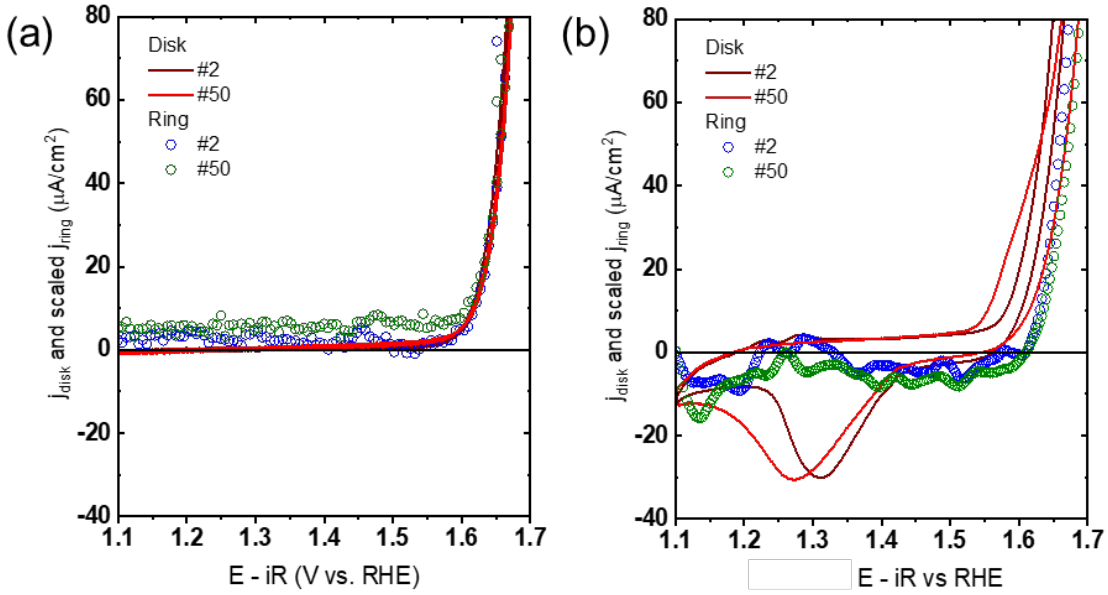

Supplementary Figure 1: Oxygen evolution of the LSMO x=0.4 (a) and PCMO x=0.33 (b) films in aqueous 0.1 M Ar-saturated 0.1 M KOH measured by rotating ring disk electrode (RRDE) cyclovoltammetry. The ring current density (circles) is measured at 0.5 V vs. RHE and only the anodic scan is shown. Electrodes were swept at 10 mV/s and rotated at 1600 rpm. For PCMO, the shift of the onset of the ring current compared to the disk current is due to the shoulder in the anodic OER scan caused by oxygen intercalation.

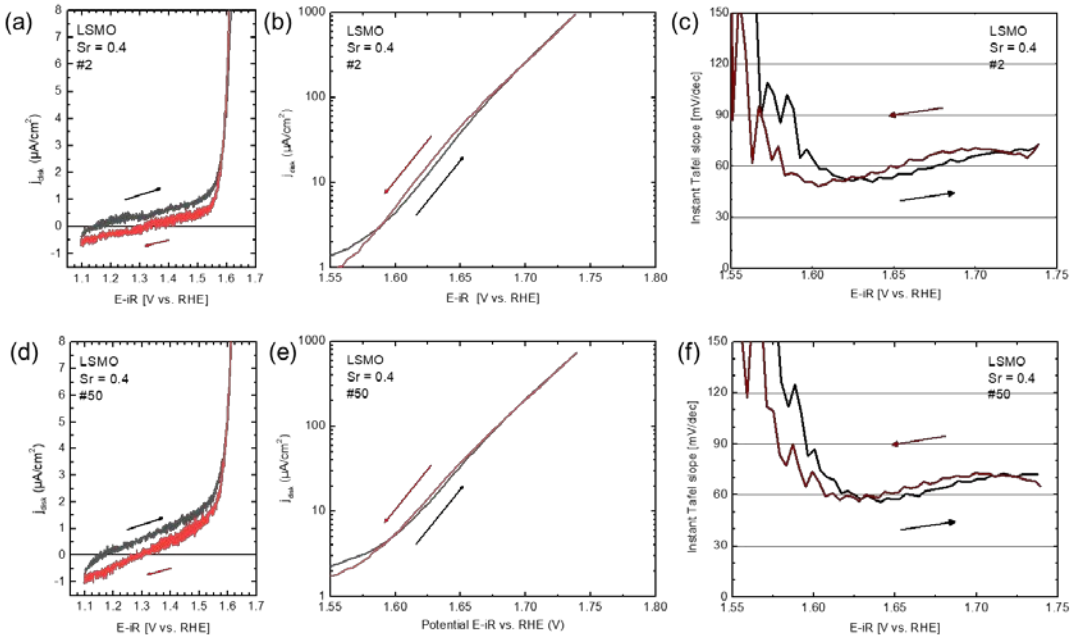

Supplementary Figure 2: Tafel analysis of the LSMO x=0.4 thin film in 0.1 M aqueous KOH solution for cycle #2 (a-c) and #50 (d-f)**.** (a,d) Cyclic voltammogram (b,e) Tafel plot and (c,f) instant Tafel slope taken for the disk current. Above 1.6 V vers RHE, the transition from capacitive to catalytic currents sets in, giving a Tafel slope of b ≈ 60-70 mV/dec. The voltage resolution of the data in panels b,c,e,f was reduced from 1 mV to 4 mV by averaging before the analysis.

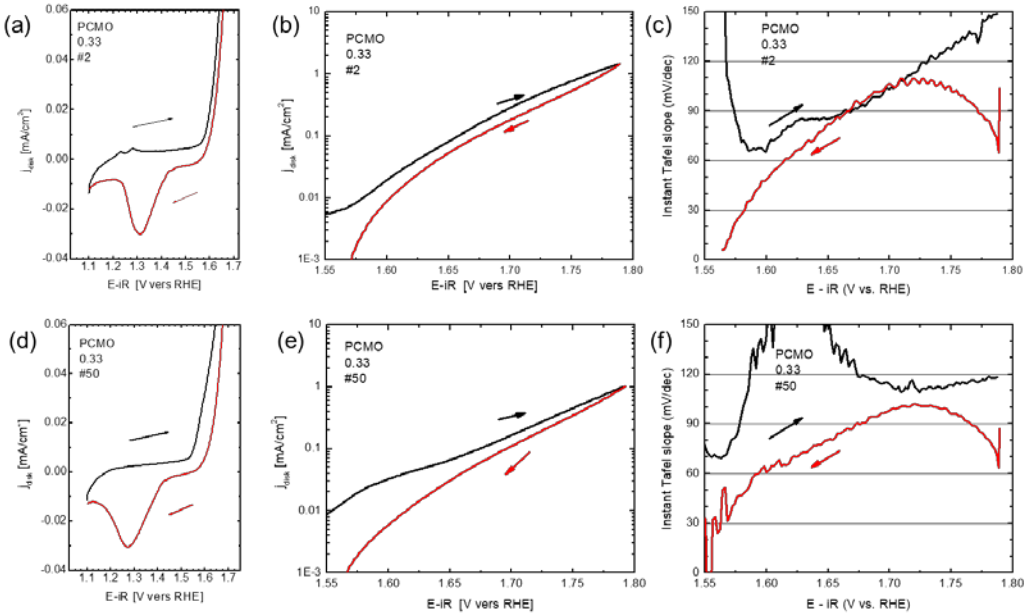

Supplementary Figure 3: Tafel analysis of the PCMO x=0.33 thin film in 0.1 M aqueous KOH solution for cycle #2 (a-c) and #50 (d-f)**.** (a,d) Cyclic voltammogram (b,e) Tafel plot and (c,f) instant Tafel slope taken for the disk current. The transition from capacitive to catalytic current above 1.6 V vers RHE is superimposed by pronounced surface redox process, leading to a peak in the Tafel slope of the anodic current at 1.6-1.65 V vers RHE for cycle #2 and at 1.58-1.68 vers RHE for cycle #50. The Tafel slope related to OER of PCMO (001) surface is strongly potential dependent and ranges between 90-120 mV/ dec. Tafel slopes for potentials above 1.75 V vers RHE are not further considered because of the large hysteresis of the current.

2. Structural characterization of epitaxial (001) oriented LSMO and PCMO electrodes in pristine state and post electrolysis

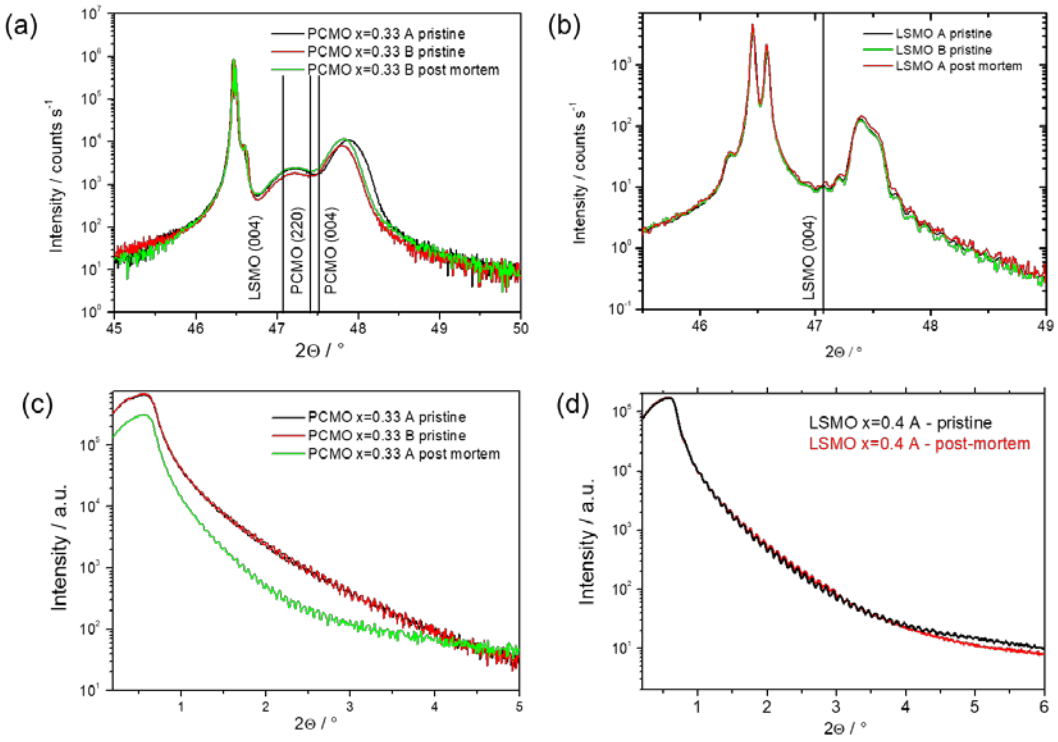

Supplementary Figure 4: X-ray diffraction and x-ray reflectivity of PCMO x=0.33 and LSMO x=0.4 epitaxial thin films, pristine and after 1 h of OER at 1.7 V vers RHE. (a) Detailed 2θ XRD scan on the (004)/(220) PCMO reflex as well as the (004) reflex of the LSMO buffer layer for two different films. (b) Detailed 2θ XRD scan on the (004) LSMO reflex for two different films. All films show out of plane compressive strain which is consistent to the in-plane tensile strain due to the misfit to the Nb:$SrTiO_3$ substrate. Peak position is not changed after electrolysis. (c,d) Reflectometry of the PCMO and LSMO films giving a thickness of 104 and 85 nm, respectively. The comparison of pristine and post mortem measurements demonstrates the high stability of the LSMO film, whereas the PCMO films shows changes in thickness and density.

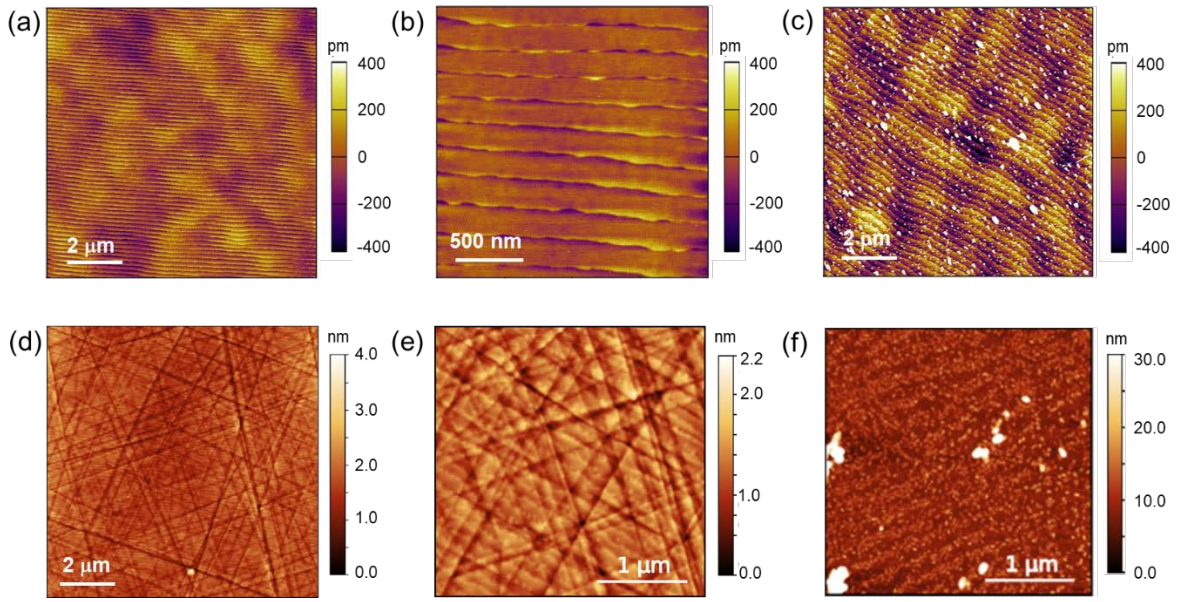

Supplementary Figure 5: Exemplary AFM images of as grown epitaxial LSMO x=0.4 (001) (a-b) and PCMO x=0.33 (001) (d-e) thin films. (c) and (f) show the surface after 50 cycles of OER between 1.1 and 1.75 V vers RHE and 7 min CA between cycle 3 and 4. Particles are reminiscent of the aqueous electrolyte containing 0.1 M KOH. The thickness of all films is 80 nm.

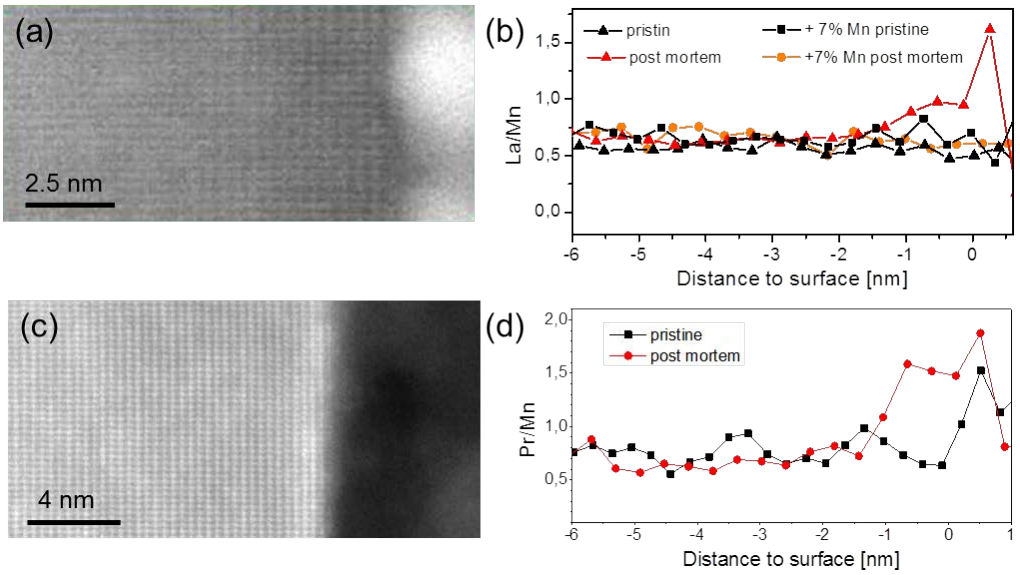

Supplementary Figure 6: Post mortem study of the surface of LSMO (001) (a,b) and PCMO (001) (c,d) films after 1h of electrolysis at a potential of 1.7 V vers RHE. a) STEM HAADF image of a post mortem LSMO film in cross section. The lamella was prepared by FIB using a PtC protection layer, where a Pt particle at the surface of LSMO is visible as a bright area on the right side of the image. (b) Line profiles of the La/Mn ratio as a function of the distance to the surface determined by STEM EELS of a pristine LSMO film, and the same film after electrolysis. Mn depletion is visible for a region of ≈ 1 nm below the surface. In addition, data for a Mn enriched off-stochiometric film is shown before and after electrolysis, in order to demonstrate reliability of our method. (c) STEM HAADF image of a post mortem PCMO film in cross section. The lamella was prepared by using an epoxy protection layer, visible as the dark region above the surface. (b) Line profiles of the Pr/Mn ratio as a function of the distance to the surface determined by STEM EELS of a pristine PCMO film, and the same film after electrolysis. Strong Mn depletion is visible for a region of ≈ 2 nm below the surface. The Pr/Mn ratio is also somewhat enhanced over the full length of the line profiles in the electrolyzed sample, due to the leaching at the two PCMO-water interfaces normal to the electron beam.

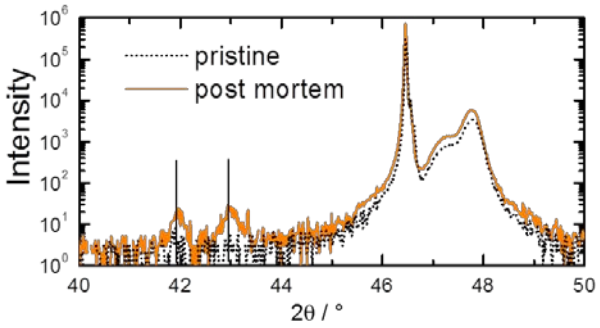

Supplementary Figure 7: Comparison of a PCMO (001) film before and after 3 cycles of voltammetry between 1.1 and 1.8 V vers RHE and 7x1 min of electrolysis at 1.5, 1.55, 1.6, 1.65, 1.7, 1.75 and 1.8 V vers RHE. The new peaks after electrolysis correspond the lattice spacings of 2.15Å and 2.1Å, respectively. The peak at 42° is close to (002) of the cubic PrO_2 structure with a= 0.539 nm.

4. TEM Lamella/Sample preparation and subsequent surface characterization

For in-situ atomic scale reactions we have fabricated ultrathin TEM lamella by a special technique based on focused ion beam (FIB) and further ion milling, avoiding damaged amorphous surface layers, as well as catalytic protection layers such as Pt[1]. Wedge shaped lamella with dimensions of 14 X 2 X 7 μm^3 were cut out of the (001) oriented PCMO and LSMO thin films using FEI Nova NanoLab 600 Dual Beam instrument.

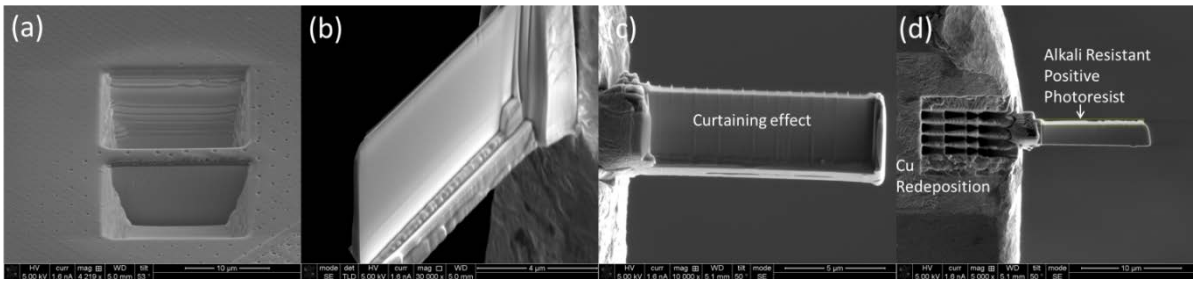

Supplementary Figure 8: SEM-FIB snapshot images of lamella preparation procedure. (a) Cut of a plate-like cross-section lamella using Alkali Resistant Positive Photoresist X AR-P 5900/4 protection layer on the LSMO surface. (b) TEM lamella after thinning procedure in FIB. (c) TEM lamella after glueing to a Cu grid using Cu redeposition technique. Because of inhomogeneous thickness of photoresist, a curtaining-like pattern is observed. (d) Finally thinned lamella with a few hundreds nm photoresist layer is still present on top of the film surface in order to protect the lamella from beam damage.

We have used a commercially available Alkali Resistant Positive Photoresist X-AR-P5900/4 (Photoresist) (http://www.allresist.de/photoresists-xar-p5900-4), deposited uniformly on the sample surface with a spin coater at 4000 rpm, during 60 sec. The coating was dried for 30 min in the oven (circulating air) at 100 ° C and then, a mask was placed in the center of the sample and exposed for 6 minutes using the UV lamp 360-450 nm. The sample was etched for 20 seconds with 10% NaOH and rinsed well in distilled H_2O, finally 20 sec H_2O in ultrasonic bath. A FIB lamella was then cut and lifted out of the protected area (Supplementary Figure 8). To avoid contamination of platinum in any aspect, TEM lamella is attached to Cu grid carefully by using Cu redeposition technique (Fig S8d). Copper is redeposited from Cu grid to attach the lamella using 30 kV accelerating voltage and 1 nA ion beam current with 1 ms dwell time. The last thinning step was done at 5 kV at ion beam current of 29 pA. Afterwards, the thickness of photoresist protective layer was about 30 nm along the whole surface of the lamella which was removed by a final Ar ion milling step by a Gatan Precision Ion Polishing System 691 (PIPS). We used 100 eV Argon ions and ion current of 0.42 µA for 20 minutes. Before inserting the lamella into the TEM, plasma etching in pure oxygen plasma was performed.

Even after the final Ar ion milling step and oxygen plasma etching we still observed a 2 nm thick amorphous layer on the top of bulk LSMO (Supplementary Figure 9). In order to confirm whether it is a damaged surface during sample preparation, residual photoresist or any kind of contamination, we have investigated this surface by electron energy loss spectroscopy (EELS) analysis. The EEL spectra is recorded with two different energy dispersions. Presence of Mn L and O K edges are clearly seen in the both spectra. In the amorphous areas, the shape of the O k edge is different from typical perovskite

oxide spectra and absence of O K prepeak indicates that reduced LSMO was formed during sample preparation. This is confirmed by the presence of Lanthanum M edge in the amorphous layer.

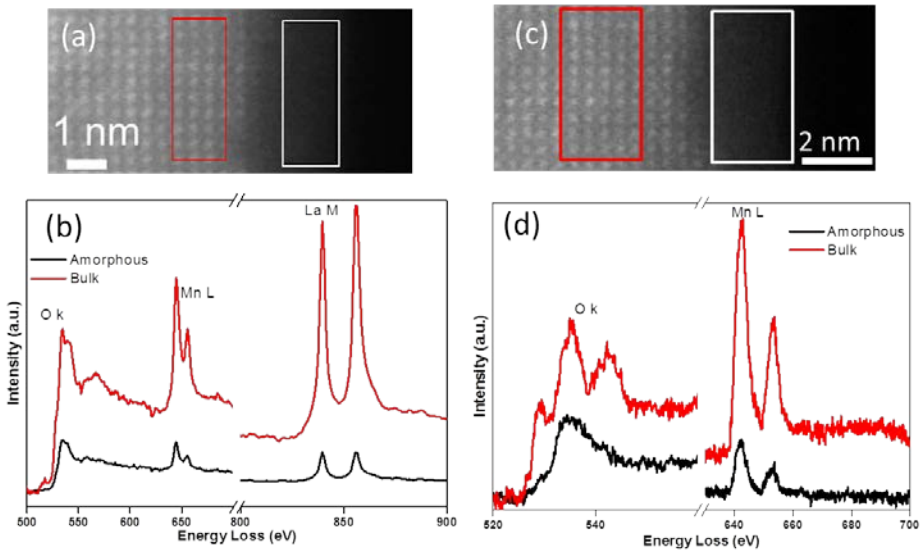

Supplementary Figure 9: Typical surface structure of a LSMO lamella after removal of photoresist by plasma cleaning with a 2 nm thick amorphous layer analyzed by STEM-HAADF (a & c) and EELS (b & d). Red rectangle marks fully crystalline bulk LSMO and white amorphous surface area, where EELS of O K-, Mn L- and La M-edges were recorded, respectively. Absence of the typical 3-fold structure of the O K- edge including the prepeak in amorphous area shows a reduced LSMO state due to preferential sputtering of oxygen by Ar ion milling.

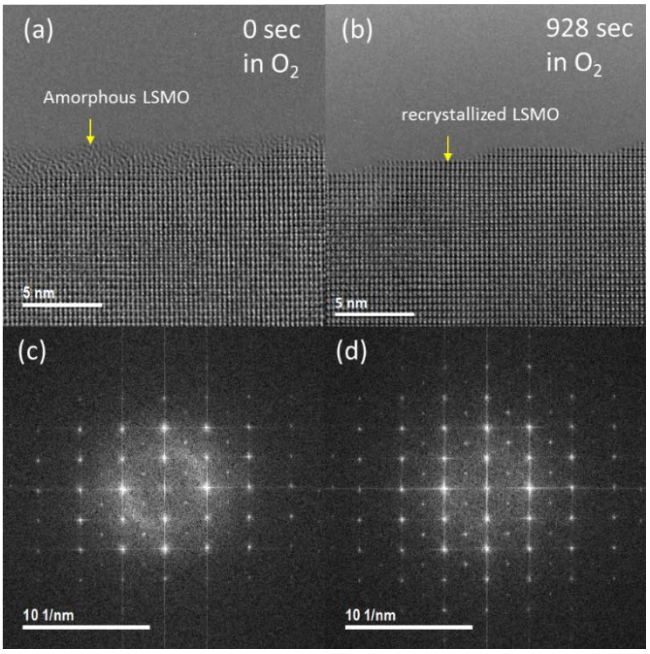

Supplementary Figure 10: HRTEM images of the pristine and recrystallized surface and their corresponding FFT's in 1 mbar O_2. (a) Thin amorphous layer at the top of LSMO surface after final thinning steps of the TEM lamella. (b) Recrystallized surface after 15 min electron beam exposure in 100 Pa of O_2. The absence of amorphous rings in (d) compared to (c) indicates complete recrystallization of amorphous LSMO on all lamella surfaces.

Similar to the procedure for PCMO x=0.33[2], we performed an electron beam induced surface recrystallization and oxidation process of amorphous LSMO under oxygen partial pressure of 1 mbar at room temperature in the ETEM. After continuous exposure to an electron-beam for about 15 minutes, amorphous LSMO was fully recrystallized with nice atomically flat surface facets showing some unit cell height step edges at the top of the surface (Supplementary Figure 10).

Following the recrystallization process, it is found that surface oxidation initially started at the amorphous edge with atomic steps or small pyramids which grows slowly. After a few minutes of exposure to an electron beam with dose rate of 13100 e/Å^{2}s in 100 Pa of O_2 single crystalline facets are formed which are served to study in-situ atomic dynamics in H_2O. The recrystallization of the amorphous layer to the crystalline flat facet after few hundred seconds is visible in Movies M08 and M09.

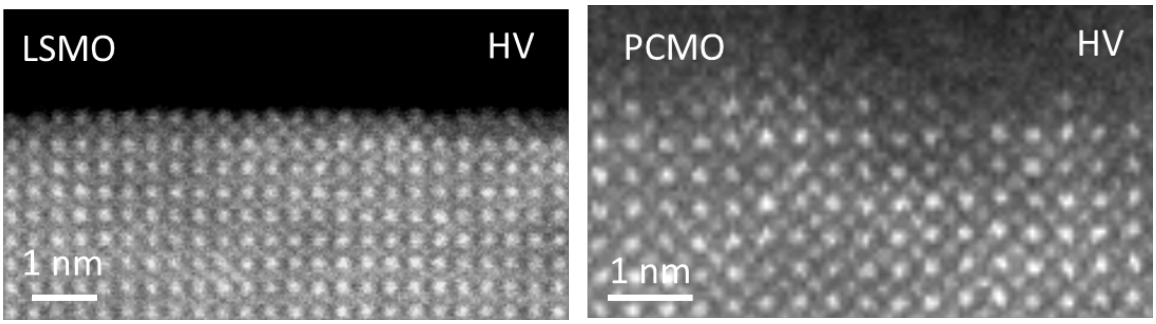

Supplementary Figure 11: STEM HAADF images of the (001) surfaces of LSMO and PCMO after imaged under HV conditions. Whereas LSMO shows a crystalline surface structure dominated by A-layer terminated areas, PCMO exhibits a disordered surface in HV, even after full crystallization in 100 Pa O_2 was achieved. LSMO is imaged in the pseudocubic [010] and PCMO in the orthorhombic [110] zone axis.

5. HRTEM image simulation by the multislice method

Multislice simulations of high-resolution TEM exit wave functions were performed using QSTEM software developed by Christoph Koch[3]. Subsequently, the aberration parameters were optimized by using a metropolis algorithm implementation to minimize the RMS of the difference between a simulated and an excerpt of the experimental image beneath the surface[4]. Finally, the optimal aberration parameters (see Supplementary Table 1) were used for the image simulations including Mn adatoms.

Parameter	Fit LSMO	Fit PCMO
C1-Defocus	-30 Å	- 63 Å
C3-Cs	-106439.86 Å	- 15817.58 Å
A1-Two fold Astigmatism A1- angle	20.23 Å 1.18 rad	68.09 Å 2.41 rad
B2-Axial coma	0 Å	8639 Å
Thickness	42 Å	43 Å
Focal spread	100 Å	100 Å
Contrast calibration factor (Sim/Exp) from first A-layer	24	-

Supplementary Table 1: Electron optical parameters determined by fitting simulated contrast to the experimental images.

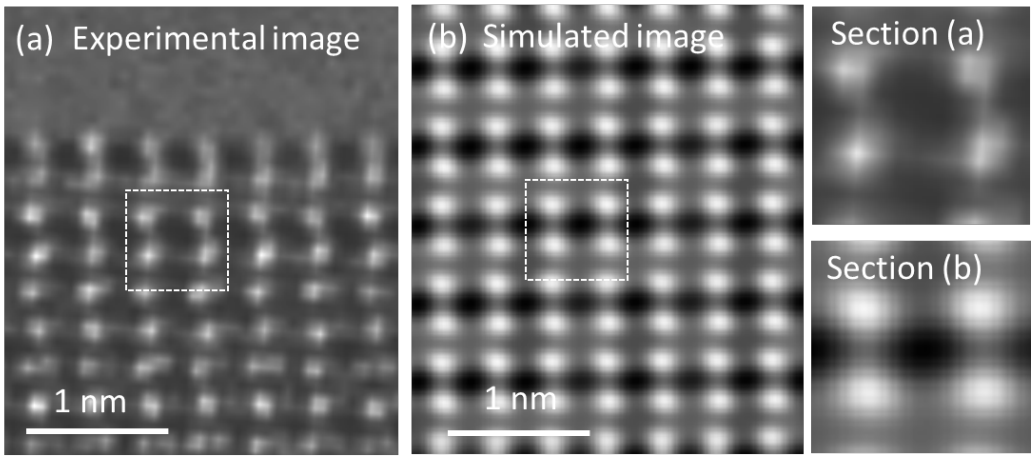

Supplementary Figure 12: Experimental image of LSMO (a) with marked section that was used for image simulation. (b) Simulated image, using the obtained fit parameters of Table S1. Left column: Cut out of the experimental image in (a) and the corresponding simulated image section of (b).

The atomic models of the simulated supercells were created with a custom python script based on the spacegroup Pbnm for PCMO with lattice parameters a = 5.42 Å, b = 5.45 Å and c = 7.67 Å[5], and spacegroup $R\bar{3}c$ for LSMO with a small rhombohedral tilt angle of 90.37° and a pseudocubic lattice constant a_c = 3.87 Å[6]. We use pseudcubic notation for LSMO in order to facilitate the comparison to PCMO. I.e. the pseudodcubic [110] zone axis and (001) surface refers to [100] zone axis and (011) surface in the rhombohedral space group. This is used for image simulation, taking the related octahedral tilting pattern into account. In order to simulate the experimentally established, homogenized occupation of A sites by La/Sr, the A-site atoms were set column by column and chosen to be Sr if the concentration of already set atoms falls below x and La otherwise. For the fitting, a cut out of an experimental image was used for the first subsurface unitcell as shown in Supplementary Figure 12. The same approach is chosen for PCMO with Pr/Ca on the A sites. This leads to a stronger local homogeneity of A-site atoms in comparison to a simple random number generation approach while still preserving the global doping concentration. We justify this local homogeneity with the absence of strong A-site contrast fluctuations in the experimental images which one would observe in the simulations in the case of a random number generated structure.

The models for both materials are constructed with the illuminating beam taken to be incident parallel to the [110] direction of the PCMO and LSMO, respectively. Different numbers of Mn adatoms occupation on the surface B sites at the upper, center and bottom edge were simulated by variation of number of Mn atoms parallel to the electron beam as well as their position. The models are exported in VESTA software for visualization.

6. Single and multiple adatom contrast (LSMO)

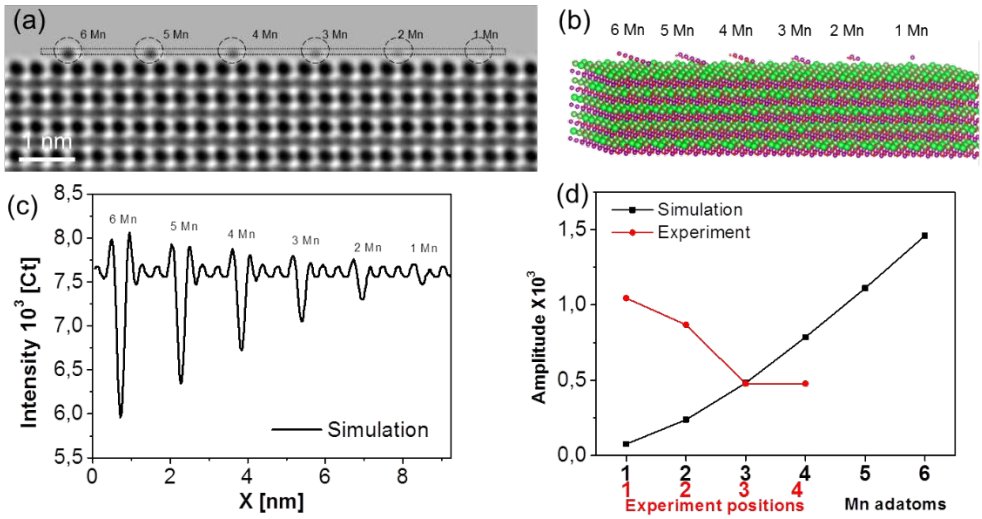

Supplementary Figure 13: Single and multiple adatom contrast. (a) Calculated image of LSMO (001) surface with bulk thickness of 4.2 nm. Black dotted circles show the positions of Mn adatom columns. (b) Visualization of the used surface structure model indicating the position of Mn adatoms columns and number of Mn adatoms at interstitial sites in a surface B-layer. (c) The corresponding line intensity profile (black dotted rectangle marked in Fig (a) for columns with 1-6 Mn adatoms. (d) Amplitude of Mn-contrast for the simulated line profiles, where the scaling factor of the simulated image was determined from the A-site contrast of the surface columns (last line in table Supplementary Table 1). In the experimentally measured contrast amplitudes for the three line profiles in Figure 3 in the main text are shown.

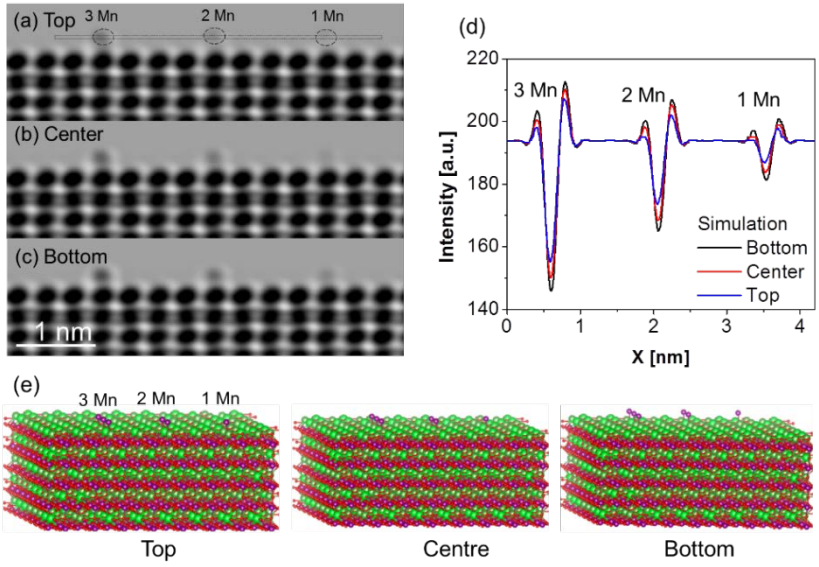

Supplementary Figure 14: Simulated images of LSMO (001) surface with a bulk thickness = 4.2 nm and 1, 2 and 3 Mn adatom per column at the top edge (a), center (b) and bottom edge (c) position at the surface. Black marked areas shows intensity of 1, 2 and 3 Mn adatoms. (d) Line profile at the dotted rectangle marked in (a) for top, center and bottom position of Mn adatoms. (e) Visualization of the surface structure with different positions of the Mn columns with respect to the upper edge of the TEM lamella.

7. Mn adatoms on Mn and La/Sr terminated surfaces (LSMO)

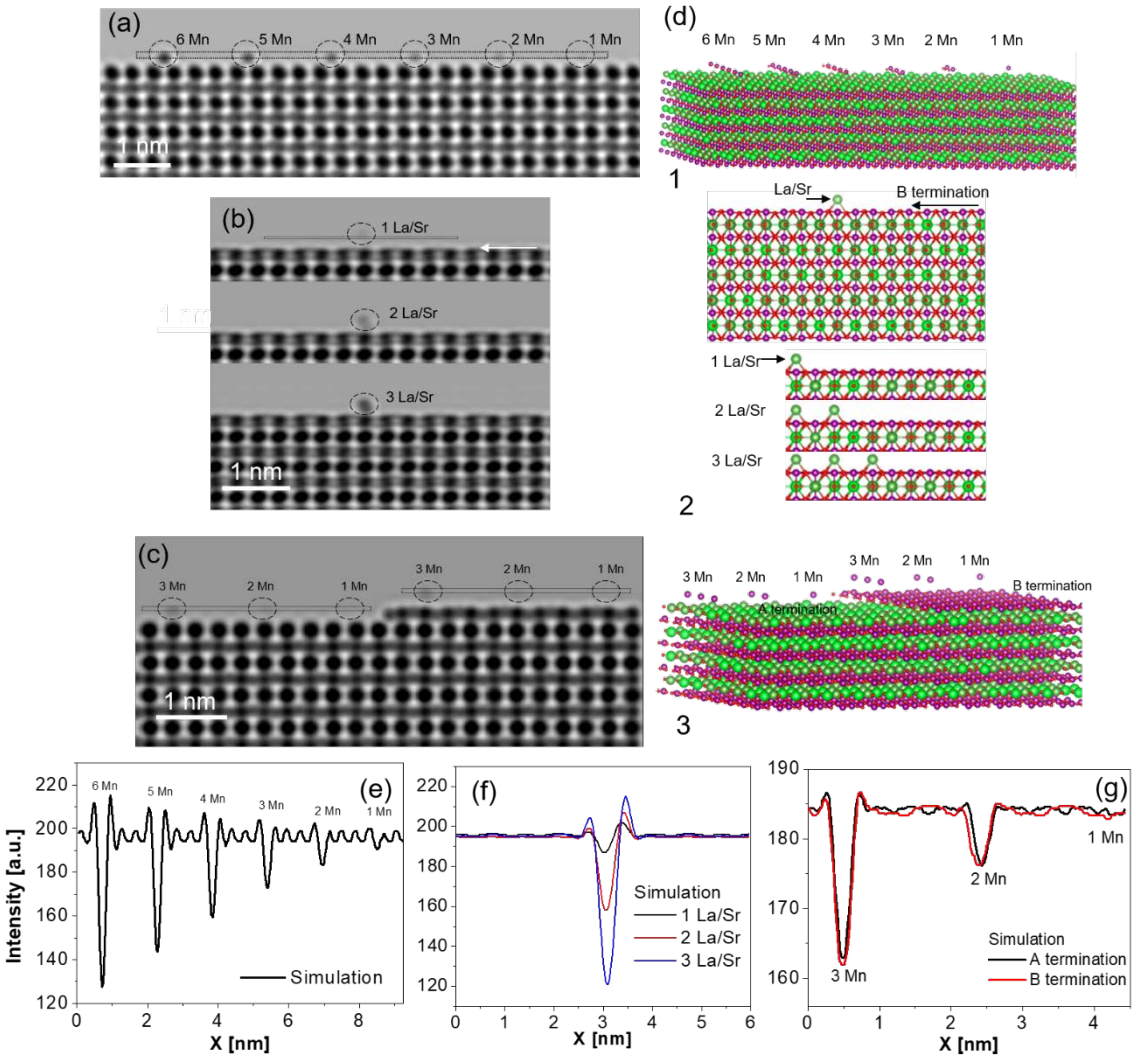

Supplementary Figure 15: Simulated image contrast of A-layer (a), Mn-layer (b) and mix layer terminated (c) LSMO (001) surfaces with a thickness of 4.2 nm and different adatoms at the surface, respectively. (d) Visualization of the crystal models used in (a,b and c) with different adatom configurations. (e) Line profiles of 1-6 Mn adatoms at interstitial positions on an A-terminated surface in (a). (f) 1-3 La/Sr adatoms on a B terminated surface marked in (b). (g) Line profiles of 1-3 Mn adatoms at octrahedral positions contrast on A- and B-terminated surfaces in (c).

8. Stability of a unit cell height surface step in H_2O

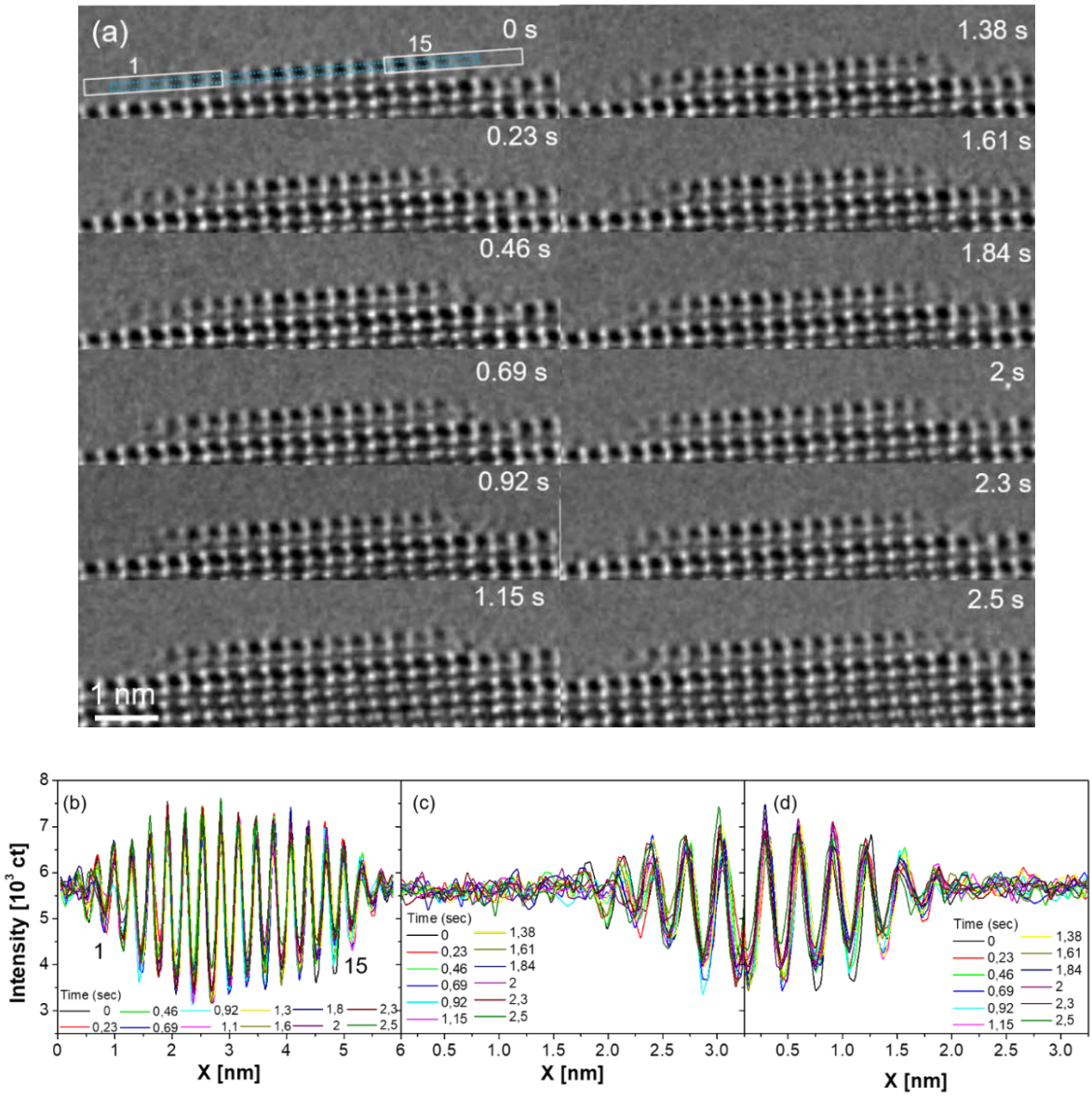

Supplementary Figure 16: Temporal sequence of HRTEM images, showing the A-site terminated LSMO 0.4 (001) surface in 0.5 Pa of H_2O (a). A static A-site terminated surface is formed, where reversible A-site dynamics is only visible at atomic step edges in the real time Movie M02. (b) The corresponding line intensity profiles for the complete unit cell height surface step at the A-site columns marked with blue rectangle in (a). (c and d) shows line profiles for left and right corners of the A-site columns at the step edge marked with white rectangles in (a).

Stable A-site cation atoms termination is observed at room temperature in the in-situ reaction in the controlled water pressure. The disordered LSMO (001) surface formed crystalline edge that is followed by stable A-termination. The HRTEM images Supplementary Figure 16 (a) are extracted with the time difference of 0.23s/frame from the Movie M02. Time resolved image sequence (a) and the corresponding line intensity profile (b) of the atomic step edge suggest that A-terminated surface is remarkably single crystalline ordered and shows atomic mobility. Line profile analysis suggests that

the atomic contrast is fluctuating on a time scale of several seconds on the same position, which can be attributed to the stable of AO terminated (001) surface in H_2O.

9. Mn surface mobility in HV

In order to compare the mobility of adatoms on the (001) surface of LSMO in absence of a liquid water layer, we continued our experiments with in-situ imaging under high vacuum conditions. Supplementary Figure 17 shows a time sequence of HRTEM images (0.23s-5.06s) of the crystalline LSMO surface at an octagon pressure of 2×10^{-5} Pa with a cold trap in the octagon, in order to further reduce the water partial pressure.

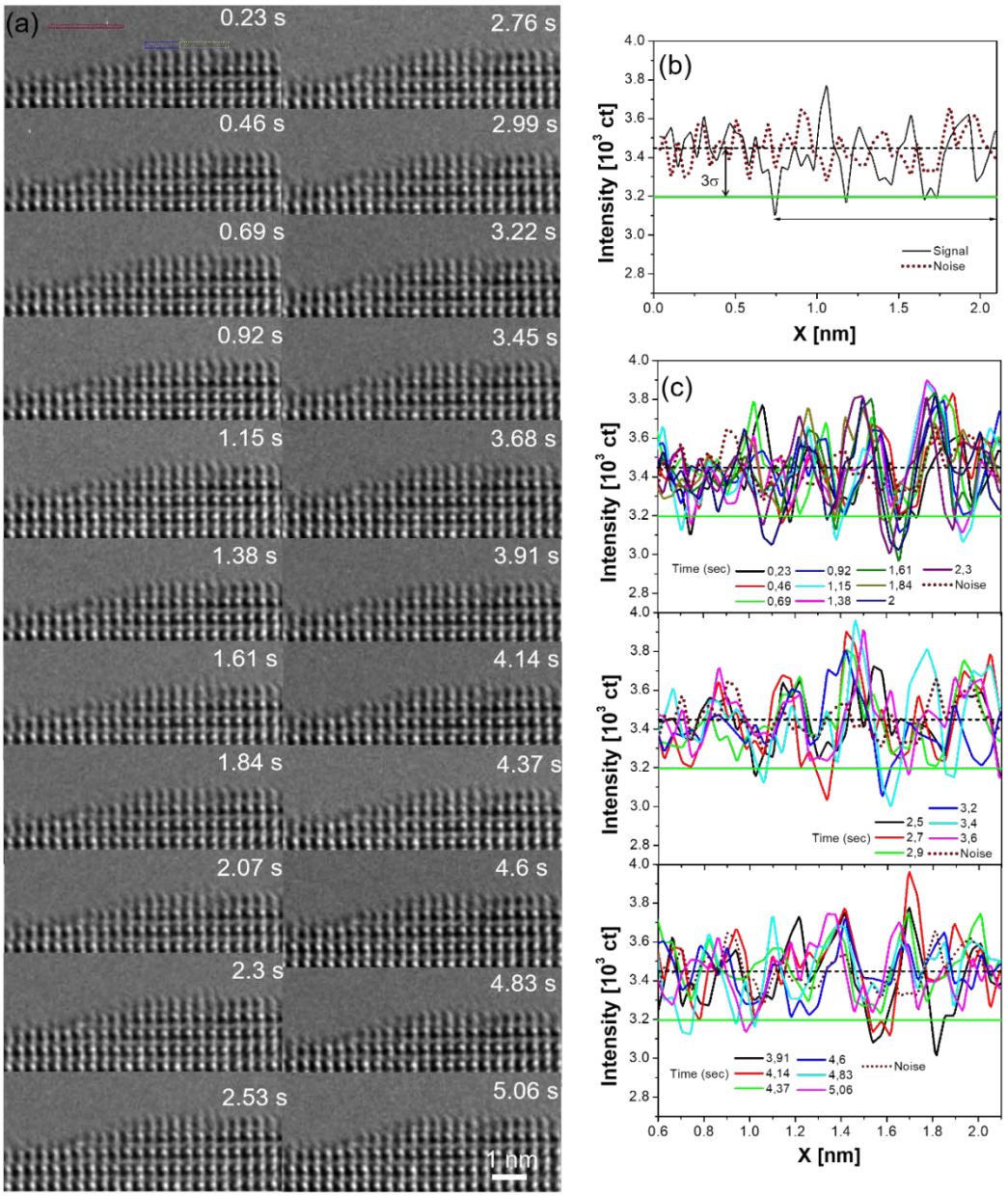

Supplementary Figure 17: (a) Time sequence (0.23s – 5.06 s) of HRTEM images of the LSMO (001) surface in high vacuum. A single crystalline LSMO (001) surface facet was prepared in O_2 and was subsequently used to study atomic dynamics in HV. The crystalline surface in HV shows mixed surface termination and is less mobile as compared to in H_2O. (b) Shows line profile at a B site position

marked as blue rectangle in the image at 0.23s. (c) Line profile of B site position (yellow rectangle) for time sequence from 0.23s-2.3s, 2.5s-3.6s and 3.9s-5.06s, respectively, where most Mn is visible. The Mn terminated areas display a more pronounced disorder compared to A site terminated areas.

The study of surface stability and atom dynamics of the LSMO (001) surface in HV are presented in Supplementary Figure 17. A stable LSMO (001) surface with mixed surface termination and a higher disorder at the Mn terminate regions is observed in HV. The surface is not changed during 10 min of e beam exposure at approximate 10,000 e-/Å^{2}s. For the comparison of Mn surface mobility we have selected a time sequence of HRTEM images from 0.23s-5.06s from the Movie M03 with 4 fps. Supplementary Figure 17 b shows a line profile of a surface area at the B-site positions marked with blue rectangle. The 3σ deviation from the average taken from the noise profile at the brown rectangle in the image at 0.23s is shown. The line profiles in (c) show line are taken from the images at 0.23s-2.3s, 2.5s-3.6s and 3.9s-5.06s, respectively, suggesting that Mn occupation of B site columns can be stable for more than 2 seconds. This also confirms that the rate of Mn surface hopping is with $r < 0.5$ s^{-1} considerably slower in HV. Long-time observation of perovskite structure of LSMO under electron beam in HV for 12 minutes shows no visible structural changes.

10. Mn surface mobility on LSMO (001) in O_2

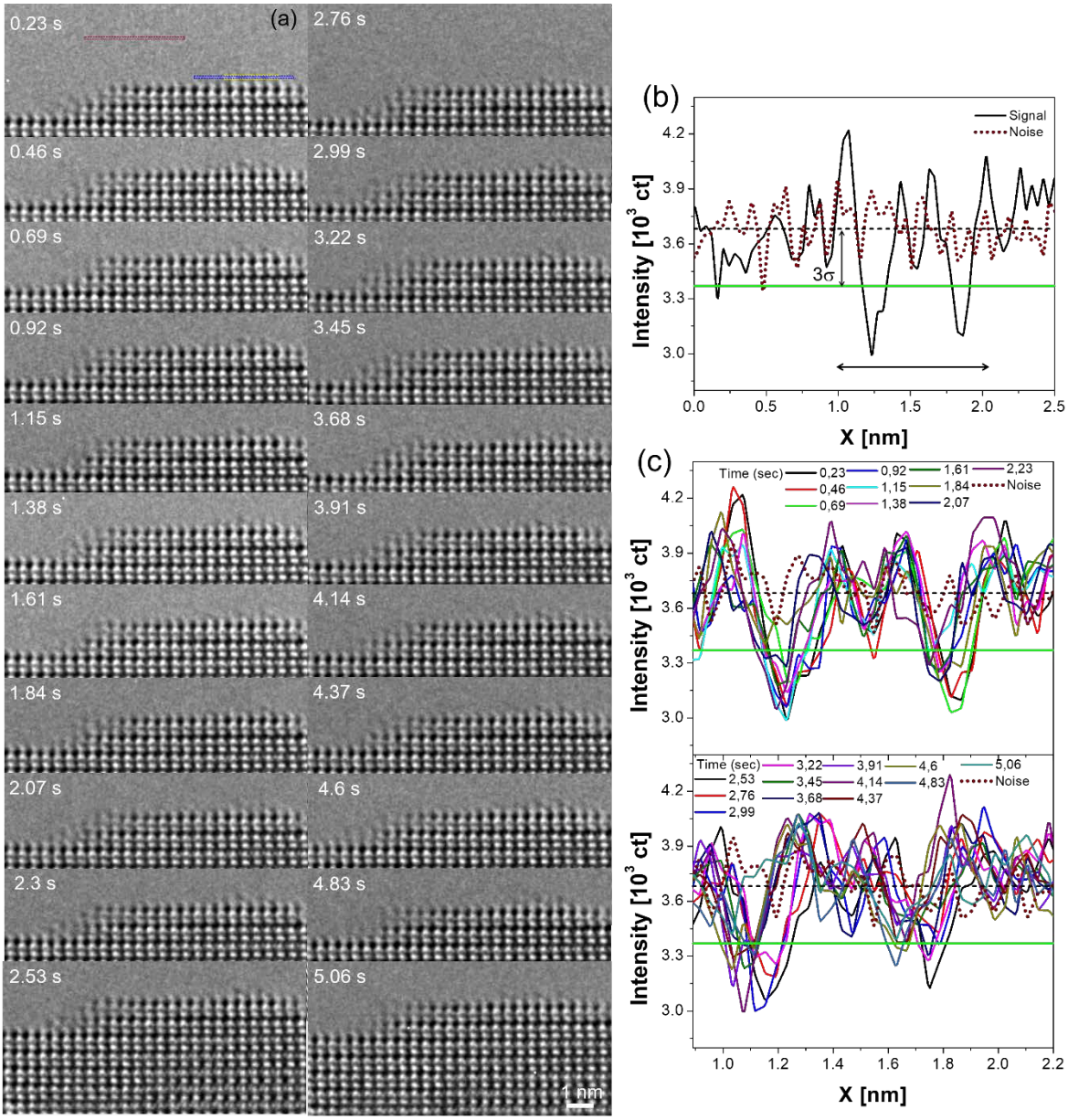

Supplementary Figure 18: (a) Time sequence of HRTEM images of a (001) LSMO surface taken at 0.23s – 5 s in 100 Pa of O_2 (Movie M04). The surface is predominantly A-site terminated. (b) shows line profile at a B site position (yellow rectangle) and noise with a 3σ line calculated from noise profile in brown rectangle in images 0.23s. (c) Line profiles at a B site position (yellow rectangle) for time sequence from 0.23s-2.3s and 2.5s-5.06s, respectively. Mn adatom sticking time is more than 3 s, i.e. hopping rate is $r \leq 0.33\ s^{-1}$

11. Mn surface mobility in N_2

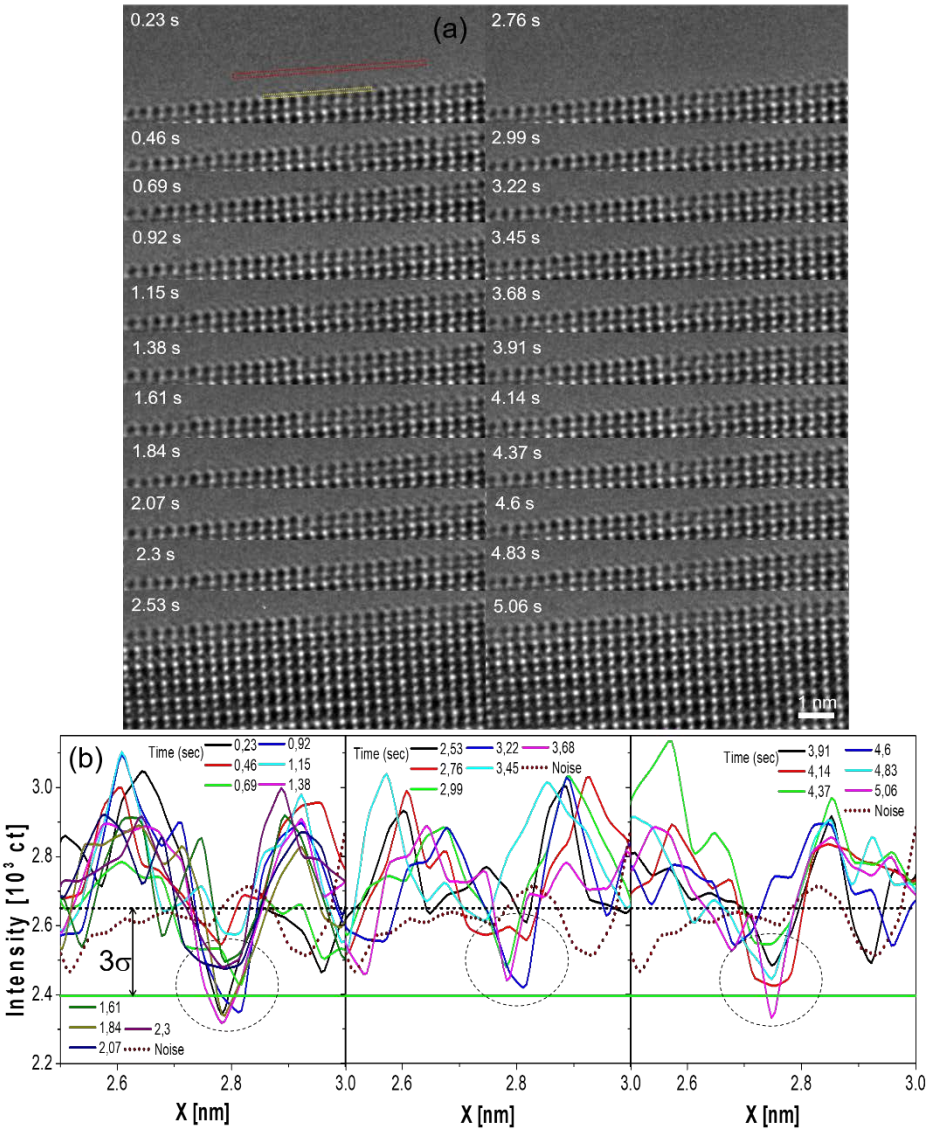

Supplementary Figure 19: (a) Time sequence of HRTEM images 0.23s – 5.06 s of a (001) LSMO surface in 10 Pa N_2. The surface is predominantly B-terminated (Movie M05). (b) Line profiles at a B-layer position (yellow rectangle) for time sequence from 0.23s-2.3s, 2.5s-3.6s and 3.9s-5s, respectively. The sticking time is close to 4s, i.e. $r \approx 0.25\ s^{-1}$. Noise 3σ is calculated from the noise profile taken at the brown rectangle in image at time 0.23s and shown as a dotted line in (b).

12. Post ETEM analysis of the Mn L and O K edges close to the surface of LSMO and PCMO

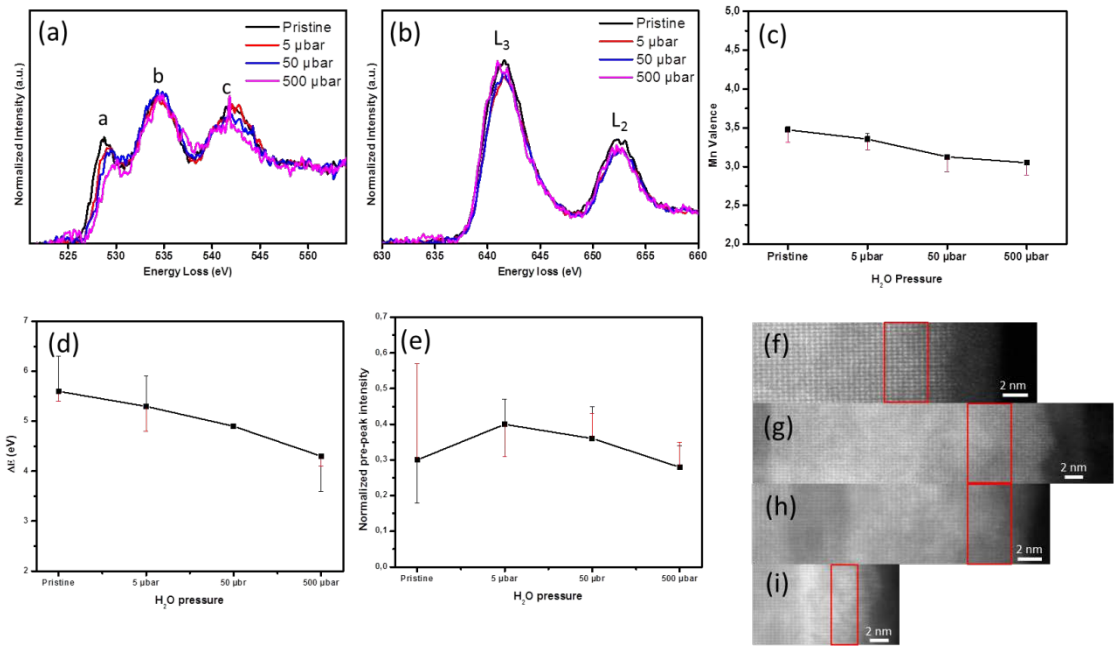

Supplementary Figure 20: Post ETEM EELS analysis at the Mn L-edge and O K-edge of LSMO film after removal of water. The O K (a) and Mn L2,3 –edges (b) spectra are taken form the area with red colored rectangles in HAADF-STEM image (f-i) for pristine and p_{H2O} = 0.5 Pa, 5 Pa & 50 Pa, respectively. (b) The Mn L3 edge maximum shows very small noticeable shift for post mortem spectra in water. The close to surface Mn valence change is shown for the pristine sample and different water pressures. (f-i) HAADF-STEM image showing the rectangles, where EELS spectra were recorded. Amorphous areas at the top of the surface which forms after switching back from H_2O to HV state of the octagon is strictly excluded from the analysis due to high amount of Carbon. (d) Energy separation calculated as the difference between positions of the second peak 'b' and the pre-peak 'a' of the O K edge as a function of increase in water pressure. (e) Normalized pre-peak intensity versus water pressure.

We have carried out an extensive investigation of the LSMO (001) surface with high resolution Scanning transmission electron microscopy – electron energy loss spectroscopy (STEM-EELS). The EELS edges shapes and chemical shifts are very sensitive towards crystal field interaction and gives information about 3d occupancy and the valence state of transition metal. Supplementary Figure 20 (a & b) shows O K and Mn $L_{3,2}$ edges corresponding to pristine LSMO surface as well as after reacted with water with pressures of 0.5 Pa, 5 Pa & 50 Pa, respectively. The Mn L edges spectra (b) exhibits two edges L3 (641-641.5 eV) and L2 (652-652.5 eV) which are the consequence of the splitting of Mn 2p states in two $2p_{3/2}$ and $2p_{1/2}$ due to spin orbit coupling. The Mn valence state in Supplementary Figure 20c is analysed by calculating the L3 to L2 ratio and calibration to the data of Varela et al[7]. Whereas there is no change between pristine and 0.5 Pa H_2O within error, a slight reduction of Mn close to the surface is observed at higher pressures.

Supplementary Figure 20 (a) shows O K edge spectra at various water pressures. O K edge spectra is the governed by the excitation of O1s electrons to the O2p unoccupied states (prepeak a), A site d states

(b) and vacuum levels (c)[8]. Empty states in the O2p band are formed due to hybridization with Mn 3d orbitals As shown in Supplementary Figure 20e, compared to the pristine state, the pre-peak a to O K edge ratio increases at 0.5 Pa and then further decreases at higher water pressure. The latter can be attributed to an increase of the filling of the O 2p states due to electron donors, such as oxygen vacancies or due to Sr leaching. It is consistent to the slight trend of Mn reduction obtained from L3/L2 ratio analysis.

The same post ETEM analysis after H_2O is performed for the PCMO (001) surface is shown in Supplementary Figure 21. Here, a pronounced Mn reduction is observed at 0.5 Pa H_2O. This is consistently obtained from analysis of L3/L2 ratio, energy separation between positions of the second peak 'b' and the pre-peak 'a' of the O K edge and normalized O K pre-edge intensity ratio. Due to the fast Mn leaching in PCMO, the interpretation of the correlation between changes in the L3 and L2 edges compared to the O K edge is not trivial.

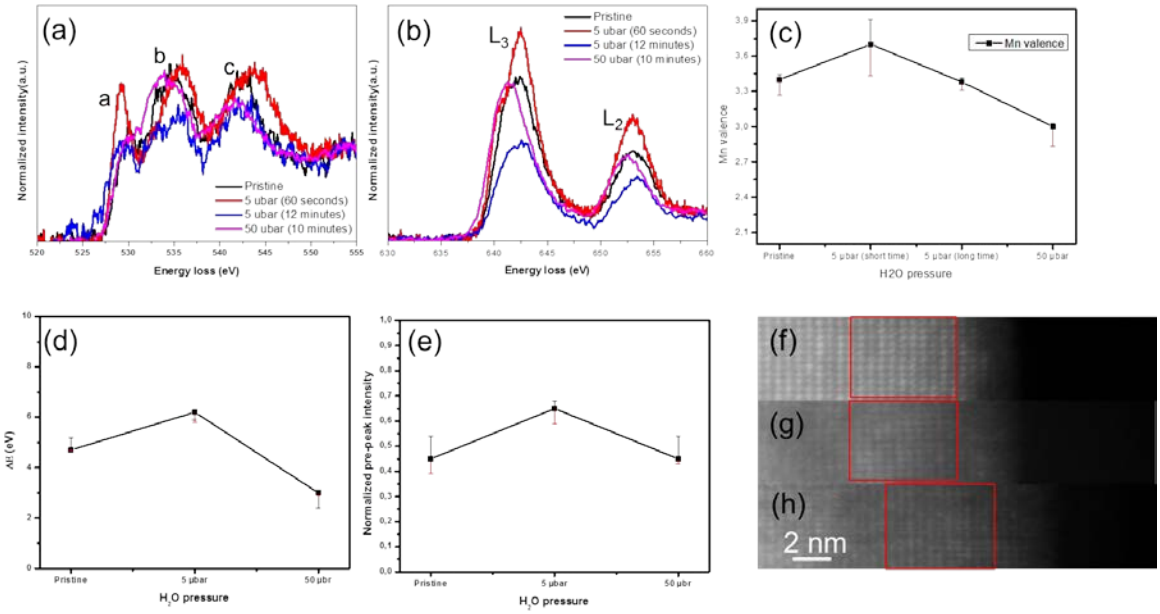

Supplementary Figure 21: Post ETEM EELS analysis of the Mn L- and O K-edges of close to surface region of the PCMO (001) film after removal of water. The spectra in O K (a) and Mn $L_{2,3}$ –edges (b) are taken from the area with red colored rectangles in HAADF-STEM image (f-h) for pristine and p_{H2O} = 0.5 Pa and 5 Pa, respectively. (c) Mn valence change from the pristine to 5 Pa water pressure. (d) Energy separation calculated as the difference between positions of the second peak 'b' and the pre-peak 'a' of the O K edge as a function of increase in water pressure. (e) Normalized pre-peak intensity versus water pressure. (f-h) HAADF-STEM image showing the rectangles where EELS spectra were recorded.

13. Formation of a condensed H_2O layer on oxide surfaces at $p \leq p_{vap}$

The thickness of a liquid water layer on a metal-oxide surface in the ETEM experiments is calculated as a function of of water partial pressure p_{H2O} by using energy balance between the surface energy of the oxide γ_s in HV, the surface energy γ_{H2O} of liquid H_2O to H_2O vapor and the adsorption enthalpy of H_2O on the oxide surface, ΔH_{ad}. This results in

(1) $$\gamma_{H2O}(\theta) - \gamma_s = \theta \Delta H_{ad}(\theta, p)$$

For the formation of the first 1-2 monolayers of liquid water, both $\gamma_{H2O}(\theta)$ as well as $\Delta H_{ad}(\theta, p)$ may depend on the coverage θ. Since experiments show that the formation of the first 2-4 monolayers of liquid water on the surface is completed for $p_{H2O} \geq 10^{-5}$ Pa[9,10,11], we restrict the calculations to the growth of liquid H_2O on a pre-formed 2ML thick water layer and approximate the water surface energy for $\theta \geq 2$ as a bulk water surface i.e. $\gamma_{H2O}(\theta = 2) = \gamma_{H2O,b}$ =0.76 J/m^2. For the pressure dependence of the adsorption energy of water on a liquid water surface, we use

(2) $$\Delta H_{ad}(\theta = 2, p) = \Delta H_{ad,b}(p) = \Delta H_{ad,b}(p_{vap}) + RTln\left(\frac{p}{p_{vap}}\right)$$

following from the Clausius Clapeyron equation and using the ideal gas law which is a good approximation for $p \leq p_{vap}$.

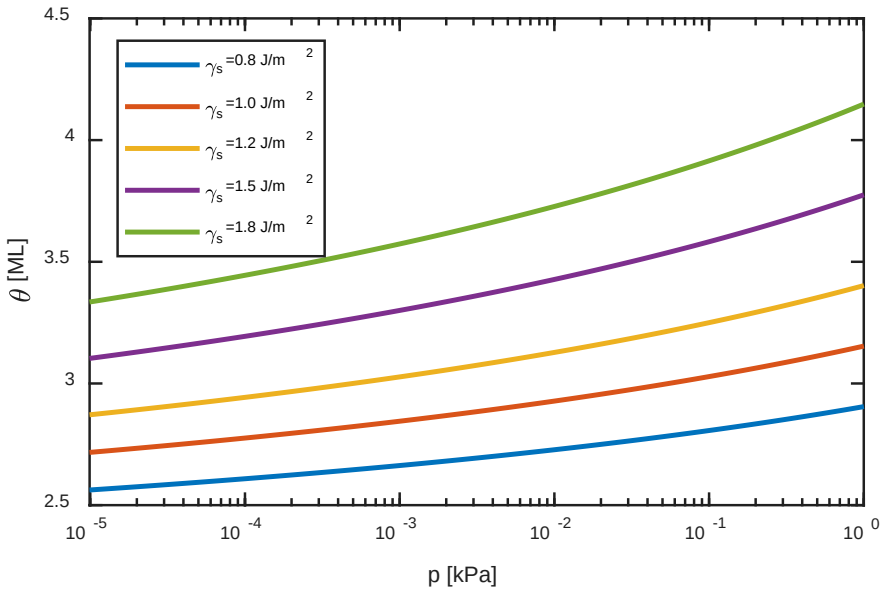

Supplementary Figure 22: Calculated coverage of oxide films with liquid water as a function of the water pressure at 25° C. The driving force for the condensation of water is the large adsorption enthalpy of H_2O on metal oxide surfaces, modified by difference between the surface energy γ_s of the oxide and that of a water surface $\gamma_{H2O,b}$ = 0.76 J/m^2.

Supplementary Figure 22 shows the surface coverage of liquid water following from Eq. (1) for different surface energies γ_s. The surface energy of perovskite oxides strongly depends on the surface termination[12]. A theoretical calculation of a (001) $LaMnO_3$ surface yields $\gamma_s \approx 0.9$ J/m^2 [ref[13]]. Independently of the choice of γ_s, the thermodynamic model shows that liquid H_2O can be condensed on top of a preformed condensed H_2O layer.

14. Covalency factor and electric transport of PCMO and LSMO

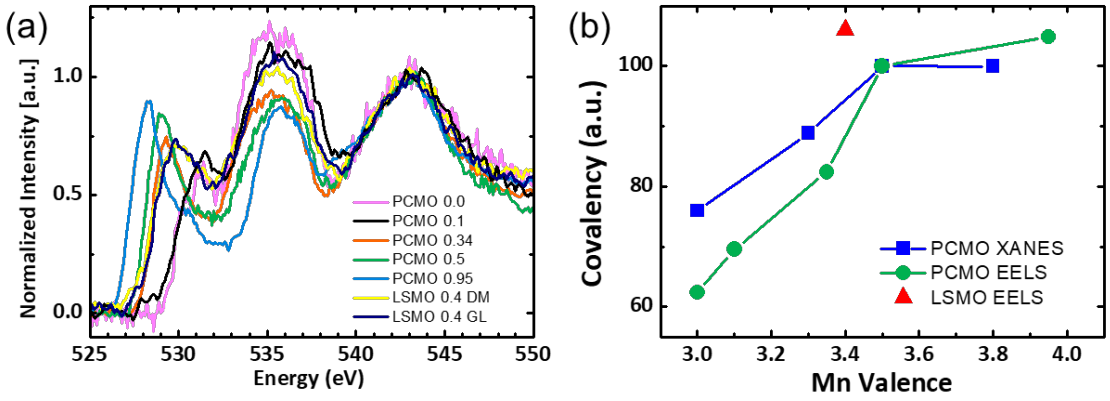

Supplementary Figure 23: a) Electron energy loss spectra (EELS) of the O K-edge PCMO x=0, 0.1, 0.34, 0.5 & 0.95 and LSMO x=0.4, respectively. Background is subtracted by polynomal fitting and intensity is normalized to the OK_c peak at energy of 543 eV. b) Covalency analysis with respect to Manganese valence. The covalency factor is obtained by integrating the OK pre-edge peak in an energy range between 525-532 eV and dividing the integral by the Mn valence. Afterwards all covalency factors are normalized to that of PCMO x=0.5, in order to visualize the trend upon doping.

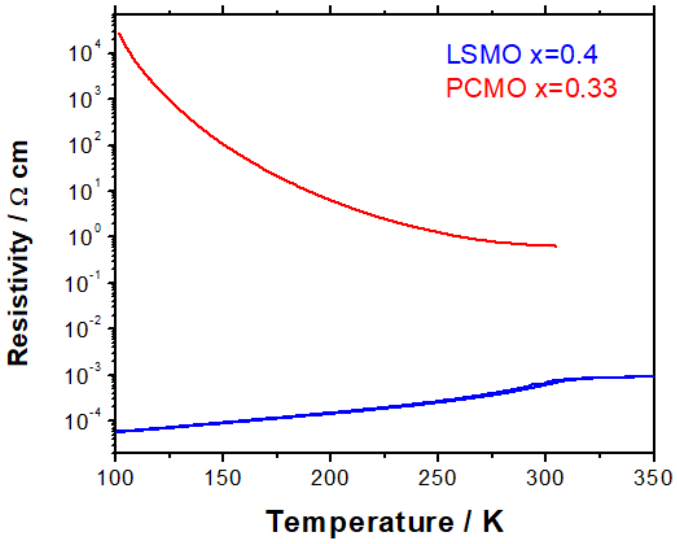

Supplementary Figure 24: Typical temperature dependent resistivity of the epitaxial (001) LSMO and PCMO films of thickness of 80 nm and 100 nm, respectively. The hopping type conductivity of PCMO x=0.33 is due to the formation of small polaron quasiparticles with an electron-phonon coupling constant of $\alpha \approx 3$ and a binding energy of about 370 meV[14]. In contrast, the metal like conductivity of LSMO x=0.4 is due to a large polaron with an electron-phonon coupling constant of $\alpha \approx$ 1-1.5 resulting a binding energy of around 100 meV at room temperature[1].

References

1. Mierwaldt, D. *et al.* Environmental TEM Investigation of Electrochemical Stability of Perovskite and Ruddlesden-Popper Type Manganite Oxygen Evolution Catalysts. *Adv. Sustain. Syst.* **1**, 1700109 (2017).
2. Roddatis, V., Lole, G. & Jooss, C. In situ preparation of $Pr_{1-x}Ca_xMnO_3$ and $La_{1-x}Sr_xMnO_3$ catalysts surface for high-resolution environmental transmission electron microscopy. *Catalysts* **9**(9), 751 (2019).
3. Koch, C. Determination of Core Structure Periodicity and Point Defect Along Dislocations. Ph.D. Thesis, Arizona State University, Tempe, AZ, (2002).
4. Rump, L. Determination of Electron Optical Aberrations by Image Matching : Implementation of a Simulated Annealing Approach. Bachelor ' s Thesis, Georg-August-Universität, Göttingen. (2018).
5. Collado, J. A. *et al.* Room temperature structural and microstructural study for the magneto-conducting $La_{5/8-x}Pr_xCa_{3/8}MnO_3$ ($0 \leq x \leq 5/8$) series. *Chem. Mater.* **15**, 167–174 (2003).
6. Zemni, S. *et al.* The effect of a cation radii on structural, magnetic and electrical properties of doped manganites $La_{0.6-x}Pr_xSr_{0.4}MnO_3$. *J. Solid State Chem.* **177**, 2387–2393 (2004).
7. Varela, M. *et al.* Atomic-resolution imaging of oxidation states in manganites. *Phys. Rev. B - Condens. Matter Mater. Phys.* **79**, 085117 (2009).
8. Sotoudeh, M. *et al.* Electronic structure of $Pr_{1-x}Ca_xMnO_3$. *Phys. Rev. B* **95**, 235150 (2017).
9. Ketteler, G. *et al.* The nature of water nucleation sites on TiO_2(110) surfaces revealed by ambient pressure X-ray photoelectron spectroscopy. *J. Phys. Chem. C* **111(23)**, 8278–8282 (2007).
10. Srinivasan, S. G. *et al.* Crystal structures, surface stability, and water adsorption energies of La-Bastnäsite via density functional theory and experimental studies. *J. Phys. Chem. C* **120**, 16767–16781 (2016).
11. Opitz, A., Scherge, M., Ahmed, S. I. U. & Schaefer, J. A. A comparative investigation of thickness measurements of ultra-thin water films by scanning probe techniques. *J. Appl. Phys.* **101**, 064310 (2007).
12. Liang Y. & Demkov A. *Interfacial Properties of Epitaxial Oxide/Semiconductor Systems. In: Demkov A.A., Navrotsky A. (eds) Materials Fundamentals of Gate Dielectrics. Page-341*. (Springer, Dordrecht, 2005).
13. Mantz, Y. A. New $LaMnO_3$ surface energy results obtained from density-functional theory. *Surf. Sci.* **695**, (2020).
14. Hoffmann, J. *et al.* Effects of interaction and disorder on polarons in colossal resistance manganite $Pr_{0.68}Ca_{0.32}MnO_3$ thin films. *Mater. Res. Express* **1**, 046403 (2015).